Manuscript prepared for Atmospheric Chemistry and Physics
with version 2.2 of the LaTeX class copernicus_discussions.cls.
Date: 21 September 2014

# Cirrus and water vapour transport in the tropical tropopause layer – Part 2: Roles of ice nucleation and sedimentation, cloud dynamics, and moisture conditions

**Tra Dinh**[1], **Stephan Fueglistaler**[1], **Dale Durran**[2], **and Thomas Ackerman**[2]

[1]Dept. of Geosciences / AOS, Princeton University, Princeton NJ 08540
[2]Dept. of Atmos. Sciences, University of Washington, Seattle, WA 98195

Correspondence to: Tra Dinh
tdinh@princeton.edu

## Abstract

A high resolution 2-dimensional numerical model is used to study the moisture redistribution following homogeneous ice nucleation induced by Kelvin waves in the tropical tropopause layer (TTL). We compare results for dry/moist initial conditions, and three levels of complexity for the representation of cloud processes: full bin microphysics and cloud radiative effects, ditto but without radiative effects, and instantaneous removal of moisture in excess of saturation upon nucleation.

Cloud evolution and the profiles of moisture redistribution are found to be sensitive to initial conditions and cloud processes. Ice sedimentation leads to a downward flux of water, whereas the cloud radiative heating induces upward advection of the cloudy air. The latter results in an upward (or downward) flux of water vapour if the cloudy air is moister (or drier) than the environment, which is typically when the environment is subsaturated (or supersaturated).

The numerical results show that only a fraction ($\sim 25\,\%$ or less) of the cloud experiences nucleation. Sedimentation and reevaporation are important, and both dehydrated *and* hydrated layers may be indicators of occurrence of cirrus clouds. The calculation with instantaneous removal of condensates misses the hydration by construction, but also underestimates dehydration due to lack of moisture removal from sedimenting particles below the nucleation level, and due to nucleation before reaching the minimum saturation mixing ratio. The sensitivity to initial conditions and cloud processes suggests that it is difficult to reach generic, quantitative estimates of cloud-induced moisture distribution in the TTL and lower stratosphere based on case-by-case calculations.

## 1 Introduction

Stratospheric water vapour plays an important role in the chemistry of the stratosphere (Solomon et al., 1986) and the radiation budget of the atmosphere (Forster and Shine,

2002; Solomon et al., 2010). Air enters the stratospheric overworld (terminology following Hoskins, 1991) predominantly across the tropical tropopause, where the exceptionally low temperatures limit the water vapour mixing ratios to a few parts per million (Brewer, 1949). However, the processes that control the dehydration as air ascends across the tropical tropopause layer (TTL, see e.g. Fueglistaler et al., 2009; Randel and Jensen, 2013) into the stratosphere remain incompletely understood. The presence of thin cirrus clouds in the TTL in the vicinity of the tropopause with a frequency of occurrence between $20\,\%$ and $50\,\%$ (Wang et al., 1996; Mace et al., 2009; Virts and Wallace, 2010) indicates that for a substantial fraction of air entering the stratosphere these cirrus clouds may be the last dehydration events.

Thin cirrus clouds in the TTL may form as remnants of outflow from deep convection (Massie et al., 2002; Wang and Dessler, 2012), or may form in-situ whereby transient temperature perturbations associated with tropical waves initiate cloud formation (Boehm and Verlinde, 2000; Immler et al., 2008; Fujiwara et al., 2009). The dehydration efficiency of these clouds due to gravitational settling of the condensates remains not well quantified. Idealised model calculations that assume instantaneous dehydration to the saturation mixing ratio have been shown to provide reasonable estimates of annual and interannual variability of water entering the stratosphere (Fueglistaler et al., 2005; Fueglistaler and Haynes, 2005; James et al., 2008), but may be systematically dry biased (Liu et al., 2010). Calculations with microphysical box models of various complexity (e.g. Gettelman et al., 2002; Ren et al., 2007; Fueglistaler et al., 2013) or one-dimensional (time-height) models (Jensen and Pfister, 2004) show that incomplete gravitational removal can indeed substantially reduce dehydration, but the reduced dimensionality of these models cannot capture the complex interplay between temperature, shear, mixing, ice crystal growth and sedimentation, and cloud-scale circulations induced by the perturbation of the radiative state due to the presence of ice crystals (Durran et al., 2009; Dinh et al., 2010, 2012).

Here, we analyse in detail the moisture redistribution by thin cirrus clouds with a cloud resolving model initialised and forced with idealised conditions typical for the

TTL. This work follows up on a case modelling study by Dinh et al. (2012), who simulated a TTL cirrus cloud with characteristics similar to observations. Our objective here is to study how efficiently thin cirrus clouds dehydrate air, and how the resulting moisture redistribution depends on the complexity of the physical processes resolved in the model. Towards this goal, we carry out three sets of model simulations which are labelled "all physics" (all-phys), "no-radiation" (no-rad) and "infinite-sedimentation" (inf-sed). For the most complete *all-phys* simulations, cloud formation due to homogeneous ice nucleation and subsequent gravitational settling of particles are calculated with detailed bin microphysics. Furthermore, the dynamical perturbations induced by the radiative heating in the presence of ice crystals are taken into account. In the *no-rad* simulations, the cloud radiative effects are neglected. Finally, for the *inf-sed* simulations, we drastically simplify the cloud microphysics by assuming that upon nucleation, particles take up all moisture in excess of saturation and immediately sediment out of the domain (at an infinite fall speed).

The model results are analysed from a Eulerian perspective of domain average water vapour profiles, and from a Lagrangian perspective of air parcels. The Lagrangian perspective is often employed in idealised studies (e.g. Fueglistaler et al., 2013), and for the interpretation of in-situ observations (e.g. Inai et al., 2013). Our numerical results show how such interpretations may be affected by problems arising from incomplete modelling of the cloud processes.

The article is organised as follows. Sections 2 describes the model and configuration of the numerical experiments. Section 3.1 describes the evolution of the clouds in the simulations. The redistribution of moisture following the occurrence of the clouds is evaluated from the changes in water vapour in the Eulerian domain (Sect. 3.2), and as following air parcels (Sect. 3.3). Section 4 summarises the results and discusses the contribution of this research to the understanding of the dehydration problem in the TTL.

## 2 Model configuration

This section describes the model configuration of six numerical experiments, namely inf-sed, no-rad and all-phys for two initial moisture profiles (dry/moist). The simulations are forced by the perturbations from a large-scale Kelvin wave and are integrated over one life cycle of a cloud. The simulations build on previous model development by Dinh et al. (2012), to which the readers may wish to refer for technical details omitted here.

### 2.1 Domain setup and forcing

All numerical simulations are in $2$D and solved using the dynamical core of the System of Atmospheric Modelling (Khairoutdinov and Randall, 2003). The simulations are subject to forcing (temperature perturbations and velocities) of a large-scale equatorial Kelvin wave (see Dinh et al. (2012, Sect. 3.2) for the mathematical and technical details). The wavelength and period of the Kelvin wave are respectively $6000$ km and $6$ d. The temporal and spatial profiles of the wave are shown in Dinh et al. (2012, Figs. 2 and 3). The model is integrated over two cycles of the Kelvin wave forcing ($12$ d) with a time step of $\triangle t = 20$ s.

The horizontal domain is equal to the wavelength of the Kelvin wave, i.e. $6000$ km. Periodic boundary conditions are applied on the lateral edges of the domain. In the vertical, the model domain extends from $z = 15$ km to $18$ km. Non-reflective open boundary conditions (Bougeault, 1983; Klemp and Durran, 1983) are applied at the top and bottom of the domain. In the horizontal, the resolution is $\triangle x = 5$ km. In the vertical, $\triangle z$ varies from $5$ m in the proximity of the cold point tropopause (CPT, at $z = 17.3$ km) to $50$ m at the top and bottom of the domain. The base-state (unperturbed) temperature profile $\tilde{T}(z)$ is taken from a sounding typical for the tropics (see Dinh et al., 2012, Fig. 1).

## 2.2 Cloud processes

Ice nucleation is computed for homogeneous freezing (Koop et al., 2000). We assume a fixed background aerosol with concentration $100\,\mathrm{cm}^{-3}$ and diameter $0.5\,\mu\mathrm{m}$. This is consistent with observed aerosol properties in the upper troposphere and lower stratosphere (Chen et al., 1998). Ice depositional growth/sublimation is solved using the bin scheme designed by Dinh and Durran (2012). The size distribution of ice crystals is resolved with $25$ bins ranging from $0.5\,\mu\mathrm{m}$ to $50\,\mu\mathrm{m}$ in diameter. Fall speeds of ice crystals are computed following Böhm (1989).

In the most complete all-phys simulations, all microphysical processes including ice nucleation, depositional growth/sublimation and sedimentation of ice crystals are explicitly resolved with the bin scheme. Additionally, we compute the cloud radiative heating that results from the absorption of radiation by ice crystals using the radiative transfer scheme described in Durran et al. (2009, their Sect. 3a). The gas phase radiative response to the temperature perturbation $T_\mathrm{c}'$ induced by the cloud radiative heating is modelled with Newtonian cooling

$$Q_\mathrm{N} = -\frac{T_\mathrm{c}'}{\gamma}. \tag{1}$$

The radiative relaxation timescale $\gamma$ is set to $20\,\mathrm{d}$ (see Hartmann et al., 2001 their Fig. 1). As further discussed in Sect. 3.1, the cloud radiative heating induces (i) a cloud-scale circulation (itself a gravity wave signal) and (ii) small-scale convective cells at the cloud top, whose buoyancy forces generate small-scale gravity waves which propagate vertically outwards from the convective layer (see also Dinh et al. (2010)). The all-phys simulations fully resolve the perturbations (in both temperature and velocities) of these gravity waves generated by the cloud radiative heating. The importance of gravity waves to the microphysical processes in TTL cirrus has also been suggested by Jensen and Pfister (2004); Spichtinger and Krämer (2013).

In the no-rad simulations, the cloud radiative heating is (artificially) turned off. Hence the Kelvin wave forcing determines all the thermodynamic conditions governing cloud formation and subsequent evolution.

In the inf-sed simulations, ice nucleation is computed based on the no-rad simulations. However, the microphysics for post-nucleation is drastically simplified by assuming instantaneous dehydration to the saturation vapour mixing ratio $q_s$ upon nucleation. Specifically, at the time and location when/where the threshold for homogeneous ice nucleation (relative humidity with respect to ice $RH_i \approx 160\,\%$ in the TTL) is reached, water vapour in excess of saturation is immediately removed by particles sedimenting out of the domain at an infinite fall speed.

## 2.3 Initial conditions

The humidity profile is initialised with a background specific humidity of $q_v = 2.09 \times 10^{-6}\,\mathrm{kg\,kg^{-1}}$ ("moist" scenario) and $1.40 \times 10^{-6}\,\mathrm{kg\,kg^{-1}}$ ("dry" scenario). These values correspond respectively to $RH_i = 120\%$ and $80\%$ around $z = 17\,\mathrm{km}$. In both scenarios, the humidity is increased smoothly from the ambient values to $RH_i = 150\%$ in a region at the centre of the horizontal domain (between $x = 2700\,\mathrm{km}$ and $3300\,\mathrm{km}$) and around the CPT. The 2D profiles of $q_v$ and $RH_i$ for the dry scenario are illustrated in Dinh et al. (2012, their Fig. 4).

These initial conditions, in combination with the Kelvin wave forcing, produce thin cirrus clouds around the tropopause that are both similar to observations (see Dinh et al. (2012) for detailed comparison between model simulations and observations) and confined within the model domain for the entire duration of simulation. In both scenarios the initial moisture profiles at the bottom of the domain ($z = 15\,\mathrm{km}$) are in general at the drier end of observed humidities. Nevertheless, for the moist scenario our profile gives a $RH_i$ similar to the in-situ measurements reported by Jensen et al. (2005, see their Fig. 1) [1]. We have chosen these profiles deliberately to ensure that in

[1] Note that the recent comprehensive instrumentation evaluation by Fahey et al. (2014) sug-

the no-rad and all-phys simulations no particles sediment out of the domain, hence the model domain captures the entire process of moisture redistribution.

Within the initially prescribed moist region near the CPT, the nucleation threshold ($\mathrm{RH_i} \approx 160\,\%$) is reached when negative temperature perturbations of the Kelvin wave arrive at the centre of the domain (at $t = 1.75$ d). In the inf-sed simulations, $q_\mathrm{v}$ decreases immediately to the saturation vapour mixing ratio $q_\mathrm{s}$ within this region at this time. In the no-rad and all-phys simulations, as ice depositional growth takes place within the clouds, $q_\mathrm{v}$ remains close to $q_\mathrm{s}$ for most of the cloudy air. Hence, in the layer where the cloud forms and ice crystals grow, the cloudy air contains more (and less) water vapour than the subsaturated (and supersaturated) environment in the dry (and moist) scenario.

## 2.4 Trajectory computation

For the Lagrangian analysis, we calculate domain-filling air parcel trajectories, initialised on a grid of $5$ km horizontally and $2.5$ m vertically. Equal spacing in geometric space (rather than proportional to mass) was chosen because we will not quantify mass fluxes, but fractions of the model domain that experience specific conditions (for example nucleation).

Trajectories of air parcels are computed using a Lagrangian parcel-tracking scheme written by Yamaguchi and Randall (2012). The scheme predicts the trajectories based on the iterative Euler-Heun method with spatially interpolated resolved-scale velocity. We use $3$ iterations to compute the resolved-scale velocity at half time steps and a third-order Lagrange polynomial interpolation to interpolate the Eulerian grid-point values (of velocities and scalars) to the parcels' locations. As the water vapour and ice along the trajectories are computed from the interpolated Eulerian grid-point values, we automatically account for the exchange of ice between different air parcels due to

gests that measurement errors may have caused overestimation in the relative humidity reported in Jensen et al. (2005).

ice sedimentation.

In the all-phys simulations, the trajectories follow the complex fluid motions which are the sum of the large-scale Kelvin wave velocities and smaller-scale radiatively induced velocities, while in the other simulations the trajectories follow only the motions from the large-scale Kelvin wave.

## 3 Results

### 3.1 Evolution of clouds in the model simulations

The cloud evolution in the $2$D domain in the all-phys simulation for the dry scenario is illustrated in the supplemental animation[2] of Dinh et al. (2012). Here Fig. 1 shows the evolution of the spatial average of the clouds in the all-phys and no-rad simulations for both the dry and moist scenarios. The difference in the background moisture of $40\,\%$ between the dry and moist scenarios leads to a much larger part of the domain being at and above saturation in the moist scenario. This results in a considerably larger cloud area in the moist scenario, which largely accounts for a difference in the domain-averaged ice mass of about $250\,\%$ between the simulations for the two scenarios (Fig. 1a). As shown in Fig. 1b, the ice number density averaged within the cloud area (not over the entire domain) is also higher in the moist scenario. In the moist scenario, the nucleation threshold is reached (and nucleation begins) at a slightly earlier time during the Kelvin wave passage when the cooling rate is higher.

In addition, Fig. 1 shows that the cloud evolution is sensitive to the cloud radiatively induced perturbations. For both the dry and moist scenarios, the radiatively induced circulation leads to an extension of the cloud area that explains to some extent the larger domain-averaged ice masses in the all-phys compared with no-rad simulations. Fur-

[2]downloadable at www.atmos-chem-phys.net/12/9799/2012/acp-12-9799-2012-supplement.zip

thermore, in both the dry and moist scenarios the all-phys simulations retain a higher ice number density after the first nucleation bursts around day $2$. The reasons for these differences between the all-phys and no-rad simulations are explained below.

Figure 2 shows the mean ice crystal radius at $t = 3.5$ d in the all-phys simulations for the dry (top panel) and moist (bottom panel) scenarios. Also shown are the cloud-scale (mesoscale) wind vectors induced by the radiative heating. This cloud-scale circulation consists of ascent centred in the cloudy region which is surrounded and balanced by subsidence. Consistent with the conservation of mass, the vertical motions are accompanied by horizontal inflow in the lower half of the cloud layer and horizontal outflow in the upper half. For detailed theoretical and numerical descriptions of the dynamics induced by a stratiform mesoscale heat source, see Durran et al. (2009); Dinh et al. (2010, 2012).

The radiatively induced horizontal motions widen the cloud tops and narrow the cloud bases. As the clouds deform into trapezoidal shapes (Fig. 2), ice crystals fall into initially clear air at the (tilted) lateral sides of the clouds (and also at the bases of the clouds). At the sides of the clouds in regions subject to horizontal inflow of environmental air, ice crystals grow to larger sizes in the moist scenario (where the ambient air is supersaturated) than in the dry scenario (where the ambient air is subsaturated).

In addition to inducing a cloud-scale circulation (as described above), the cloud radiative heating destabilises a thin layer at the cloud top in the all-phys simulations. Soon after the first burst of ice nucleation, small-scale convection develops and causes turbulent mixing and ice nucleation in the destabilised layer. On the other hand, the same layer in the no-rad simulations is stable and does not experience ice nucleation. Since the ice particle number density nucleated in the destabilised layer in the all-phys simulations is similar to that in the rest of the cloud, the average number density (Fig. 1b) is similar in the all-phys and no-rad simulations between day $2$ and $3$, while the total ice mass (Fig. 1a) and the total number of particles (not shown) are larger in the all-phys simulations.

In our simulations, the ice number concentrations (Fig. 1b) are sufficiently high such

that the distribution of in-cloud relative humidities maximises at $100\,\%$ (Fig. 3). This means that the largest fraction of the cloudy air is maintained close to saturation throughout the cloud lifetimes. Larger departures of in-cloud relative humidities from $100\,\%$ occurs in regions subject to mixing with the environment and/or where the ice number concentration is low. In the no-rad simulations, initially cloud-free air becomes cloudy only at the base of the clouds as the ice crystals fall. In the all-phys simulations, both the cloud circulation and the convective turbulence at the cloud tops enhance mixing of environmental air into the clouds. As a consequence, the frequency of in-cloud supersaturation in the all-phys run is lower than in the no-rad run for the dry scenario (where the ambient air is subsaturated). Conversely, the frequency of in-cloud supersaturation in the all-phys run is higher than in the no-rad run for the moist scenario (where the ambient air is supersaturated).

### 3.2 Cloud-induced redistribution of moisture

Figure 4 summarises the results of all model simulations in terms of the change in the water vapour mixing ratio profile. In the figure we use the notation $[q_{\mathrm{v}}^{\mathrm{i}}]$, $[q_{\mathrm{v}}^{\mathrm{f}}]$ and $[\triangle q_{\mathrm{v}}]$ to denote the averages over the horizontal domain of the initial and final $q_{\mathrm{v}}$ profiles, and of the change in $q_{\mathrm{v}}$ profile (final minus initial).

Recall that the model domain has been designed to capture all the cloud-induced moisture redistribution in the all-phys and no-rad simulations. For the inf-sed simulations, ice crystals are removed instantaneously without evaporating at lower layers, and the domain-averaged water vapour is not conserved. The lack of hydration at lower levels in the inf-sed simulations is thus not surprising per se. Rather, of interest here is the question to what extent the strongly simplified inf-sed calculation captures the dehydration induced by the cloud.

In the no-rad simulations (for both the dry and moist scenarios), dehydration ($[\triangle q_{\mathrm{v}}](z) < 0$) occurs within the initially prescribed moist region in the centre of the

domain. The magnitude of dehydration in the dehydrated layer increases with the initial available moisture (larger in the moist scenario). The processes of ice nucleation, depositional growth, followed by sedimentation and sublimation consistently lead to downward transport of water vapour in the no-rad calculation. As a consequence of ice sedimentation, the dehydrated layer lies above the hydrated layer.

The vertical integral of $[\triangle q_{\mathrm{v}}]$ over the dehydrated layer (i.e. excluding the areas that have been moistened) is more negative in the no-rad simulations than in the inf-sed simulations. In the inf-sed simulations, dehydration starts and stops instantaneously at the time when the nucleation threshold is reached. In our configurations the nucleation threshold is reached before the minimum temperature of the Kelvin wave passage. Hence, in the no-rad simulations, additional dehydration is obtained due to growth of newly formed ice crystals as temperature continues to decrease after nucleation. Furthermore, in the no-rad simulations, dehydration occurs both inside and below the layer in which ice nucleation occurs. Below the region of ice nucleation, dehydration occurs as ice crystals fall into initially supersaturated but ice-free air and grow from the available moisture.

Figure 4 shows that the effect of the cloud radiatively induced circulation on the moisture distribution is sensitive to the initial moisture profiles. For the dry scenario, in the all-phys simulation, a thin layer between $z = 16.9$ km and $17.1$ km becomes dehydrated (Fig. 4a and b), but not all of the water removed from the dehydrated layer is transported downward. In fact, a region above the dehydrated layer has been moistened (in which $[\triangle q_{\mathrm{v}}] > 0$) and the integral of $[\triangle q_{\mathrm{v}}]$ in this hydrated layer is $69$ % of the mass of water vapour loss from the dehydrated layer. In other words, $69$ % of the water from the dehydrated layer has been transported upward and the remaining $31$ % has been transported downward by ice sedimentation. Thus, the direction of the net water vapour flux is upward in the all-phys simulation in the dry scenario. On the other hand, for the moist scenario (Fig. 4c and d), the direction of the net water vapour flux is downward, and the mass of water vapour removed from the dehydrated layer is enhanced (by about $45$ %) in the all-phys simulation compared with the no-rad simulation.

For both the dry and moist scenarios, the radiatively induced ascent advects the cloudy air upwards. The direction of the water vapour flux associated with this upward advection of the cloudy air is sensitive to the vapour content of the cloudy air relative to the environment. When the cloud is surrounded by drier environmental air (in the dry scenario), upward advection of the cloudy air (which contains more water vapour than the environmental air) results in an upward flux of water vapour. On the other hand, when the cloud is surrounded by moister air (in the moist scenario), upward advection of the cloudy air (which is close to saturation while the environment is weakly supersaturated) results in a downward flux of water vapour.

To separate the advective tendencies from the impacts on the moisture profiles of microphysical processes, we compute the accumulative mass of water associated with ice-to-vapour exchange during the model integration (Fig. 5). The exchange mass between vapour and condensates is recorded at the time and location when/where (de)hydration occurs (not at the end of the model integration). With the advective tendencies excluded, Fig. 5 shows that microphysical processes consistently lead to dehydration in the upper half of the cloud layer (in contrast to Fig. 4b where the advective tendencies result in hydration above $17.1$ km in the all-phys simulation for the dry scenario). A comparison between the no-rad and all-phys profiles in Fig. 5 shows that the radiatively induced perturbations enhance the impact of cloud microphysics in redistributing the moisture profiles. This holds in terms of both the magnitude and the thickness of the (de)hydrated layers.

### 3.3 Lagrangian analysis

The Lagrangian analysis is based on the domain-filling trajectories as described in Sect. 2.4. The trajectories begin at the same initial grid points in the different model calculations, but they evolve differently in the all-phys simulations and those with reduced physics. The trajectories are the same in the no-rad and inf-sed simulations where they follow the flow in the large-scale Kelvin wave.

Parcels travelling along the trajectories are deemed to have dehydrated (by the formation and growth of ice crystals) or hydrated (by the sublimation of ice crystals falling into the parcels) if the magnitude of the specific humidity change ($\delta q_{\mathrm{v}}$, final minus initial specific humidity of the air parcels) exceeds $\epsilon = 5 \times 10^{-8}\,\mathrm{kg\,kg^{-1}}$. In the absence of mixing, only the source/sink terms associated with microphysical processes (non-advective tendencies) contribute to $\delta q_{\mathrm{v}}$ along the trajectories. However, diffusion and numerical errors (associated with interpolation in the Lagrangian parcel calculation, see Sect. 2.4) inevitably require that we allow for some margin $\epsilon > 0$ (as given above). The "dehydration" and "hydration" criteria can be defined as respectively $\delta q_{\mathrm{v}} < -\epsilon$ and $\delta q_{\mathrm{v}} > \epsilon$. Using the same margin $\epsilon$, the "cloud" criterion is defined as $q_{\mathrm{i}} > \epsilon$ at any time during the period of integration, where $q_{\mathrm{i}}$ is the ice mixing ratio along the parcels' trajectories. The cloud criterion identifies the parcels that pass by the cloud at some point during the period of integration.

Figure 6 and the supplemental animations show representative trajectories of (de)hydrated air parcels in the no-rad and all-phys simulations for both the dry and moist scenarios. Comparison between the no-rad and all-phys runs shows that trajectories of air parcels are significantly modified by the motions induced by the cloud radiative heating. In addition, notice in the animations that dehydrated parcels enter the clouds at earlier times than hydrated parcels. Dehydrated parcels enter the clouds during periods of ice growth, whereas hydrated parcels enter the clouds during periods of ice sublimation. Because of ice sedimentation, dehydrated air parcels tend to be located above hydrated parcels. In the moist scenarios, there is a near saturated layer separating dehydrated air (above) from hydrated air (below). Ice crystals fall through this layer without significant growth and/or sublimation. Air parcels that pass through the cloud in this near saturated layer satisfy the "cloud" criterion but do not dehydrate or hydrate significantly. This illustrates that the set of dehydrated and hydrated air parcels is a subset of the set of cloudy air parcels.

Using the above definitions for cloudy, dehydrated, and hydrated air parcels, below we compute (i) the fraction of the cloud that experiences nucleation, and (ii) the statis-

tics of the change in water vapour of an average (typical) air parcel passing by the cloud over the course of the integration.

### 3.3.1 Nucleation

Here we calculate the fraction of the cloud that experiences nucleation. The calculation is performed separately for the dry and moist scenarios. In the inf-sed runs, there is virtually no cloud because all ice crystals are assumed to fall out instantaneously. Thus the cloudy air is defined based on the no-rad and all-phys calculations. Let $N_{\mathrm{c}}$ denote the number of air parcels that satisfy the cloud criterion ($q_{\mathrm{i}} > \epsilon$ at any time during the period of integration) in the no-rad and/or all-phys runs. This set of parcels is referred to as "cloudy" air parcels.

In the inf-sed simulations, by construction all air parcels that experience nucleation dehydrate, and there is neither dehydration nor hydration for air parcels that do not experience nucleation. Since all thermodynamic conditions are identical in all model calculations up to the nucleation time, the set of air parcels that experience nucleation in the inf-sed runs is the same as those that experience nucleation in the no-rad runs. In the all-phys runs, additional, subsequent ice nucleation takes place in the destabilised layer at the cloud top due to turbulent mixing (as explained previously in Sect. 3.1).

Let $N^{-}_{\text{all-phys}}$ and $N^{+}_{\text{all-phys}}$ denote the number of (de)hydrated air parcels (satisfying the (de)hydrated criteria) for the all-phys run. The subscript is replaced by "no-rad" and "inf-sed" to refer to the two simplified model runs. The fraction of the cloud that experiences nucleation as a direct response to the imposed forcing (no cloud radiative-dynamical feedbacks) is given by the fraction $N^{-}_{\text{inf-sed}}/N_{\mathrm{c}}$, which is $0.26$ and $0.14$ in respectively the dry and moist scenarios (see Table 1). In other words, only $26\,\%$ (and $14\,\%$) of the cloud experiences nucleation as a direct response to the imposed forcing in the dry (and moist) scenario.

Furthermore, as also shown in Table 1, the inf-sed calculation underestimates dehydration compared to both the no-rad and all-phys calculations. In fact $N^{-}_{\text{inf-sed}}$ is $84\,\%$ (and $58\,\%$) of $N^{-}_{\text{no-rad}}$ in the dry (and moist) scenario. In other words, $16\,\%$ (and $42\,\%$) of

dehydration in the no-rad simulation occurs outside of the nucleation region in the dry (and moist) scenario. Dehydration occurs below the nucleation region as ice crystals fall into initially cloud-free air that is supersaturated but not sufficiently moist to allow ice nucleation. The error in dehydration is even larger when the inf-sed calculation is compared with the all-phys calculation: $N^{-}_{\text{inf-sed}}$ is $60\,\%$ (and $30\,\%$) of $N^{-}_{\text{all-phys}}$ in the dry (and moist) scenario.

The notable conclusion is that most air parcels that constitute the cloud never experience nucleation. Rather, post-nucleation processes including ice growth and sublimation, and gravitational settling of particles relative to the motion of the gas phase account for most of the "cloud." Furthermore, nucleation in the inf-sed run (a direct response to the forcing neglecting most cloud physics) not only misses the hydration, but also considerably underestimates the dehydrated area of the cloud.

### 3.3.2 Changes in water vapour along trajectories

Figure 7 shows the histograms of $\delta q_{\text{v}}$ for all model runs evaluated separately for the dry (left panel) and moist (right panel) scenarios. In the figure, the total number of counts over all $\delta q_{\text{v}}$-bins is the same among the model runs (all-phys, no-rad and inf-sed) and is equal to $N_{\text{c}}$ (defined in Sect. 3.3.1).

The figure shows that the distribution of $\delta q_{\text{v}}$ is sensitive to the initial conditions (dry versus moist). In the dry scenario, the all-phys simulation gives a bi-modal distribution (with peaks at large dehydration and hydration). The no-rad simulation captures the key features of this distribution, but has a third mode centred at zero. By construction, the inf-sed calculation has only trajectories that either dehydrate, or are never in the cloud field. Of interest is that in the inf-sed calculation the maximum and average water loss are smaller than in the other two calculations, a point we will return to below.

For the moist scenario, the distribution function of the all-phys run is concentrated at small $|\delta q_{\text{v}}|$ values, in contrast to the bimodality at large (de)hydration values in the dry scenario. This difference between the dry and moist scenarios can be explained from the difference in the initial moisture profiles. In the layer below the region where the

cloud forms, with decreasing height temperature increases and hence $RH_i$ decreases. Ice crystals fall through the region where $RH_i$ transitions from positive to negative (i.e. where the air is near saturation) without significant growth and/or sublimation. This near saturated region is thicker in the moist scenario (compare the thickness of the transition layer between dehydrated and hydrated air in the supplemental animations for the dry and moist scenarios).

The left panels in Fig. 8 compare the changes in specific humidity of air parcels in the inf-sed runs versus those in the all-phys runs for the dry (top panel) and moist (bottom panel) scenarios. The joint histograms (Fig. 8a and Fig. 8c) show a large number of air parcels for which the specific humidity is essentially unchanged in the inf-sed runs, but significant dehydration or hydration occurs in the all-phys runs. In addition, for dehydrated air parcels, $\delta q_\mathrm{v}$ is more negative in the all-phys than inf-sed calculations in both the dry and moist scenarios (the data for $\delta q_\mathrm{v} < 0$ lie above the one-to-one line in Fig. 8a and Fig. 8c). In other words, dehydrated parcels dehydrate more in the all-phys calculation. In the inf-sed runs, the immediate fallout of ice crystals limits dehydration to the saturation mixing ratio $q_\mathrm{s}$ at the nucleation time. Further dehydration does not occur in the same air parcels because the temperature never drops sufficiently low to bring the relative humidity above the nucleation threshold again. In the all-phys runs, dehydration continues after nucleation due to growth of ice crystals, and dehydration up to $q_\mathrm{s}$ at the minimum temperature of the Kelvin wave passage can be obtained.

The right panels in Fig. 8 show the joint histograms of $\delta q_\mathrm{v}$ comparing the no-rad with all-phys calculations for the dry (top panel) and moist (bottom panel) scenarios. Comparison between the top and bottom panels shows that the initial conditions play a major role for the result. In the dry scenario (Fig. 8b), the bulk of air parcels in the two simulations experience relatively similar changes in specific humidity, namely either a dehydration of about $-1.0 \times 10^{-6}\,\mathrm{kg\,kg^{-1}}$, or a hydration of about $+0.5 \times 10^{-6}\,\mathrm{kg\,kg^{-1}}$. The remainder of the joint histogram is dominated by parcels that are either dehydrated or hydrated in the all-phys run but for which $|\delta q_\mathrm{v}| < \epsilon$ in the no-rad run. The enhanced magnitude of the change in the water vapour profile in the all-phys compared with

no-rad simulations (Fig. 5a) is explained by an increased cloud area (hence larger number of (de)hydrated air parcels, as shown in Table 1) in the all-phys simulation. For the moist scenario, the joint histogram (Fig. 8d) is dominated by a large number of hydrated parcels in the all-phys run for which there are no significant changes in specific humidity in the no-rad run. In the all-phys simulation, many air parcels become hydrated as ice crystals fall into the initially ice-free air at the tilted lateral sides of the cloud (see Fig. 2b). In the no-rad simulation, initially ice-free air may become cloudy only at the cloud base. In addition, there is a clear deviation of the histogram from the one-to-one line (see Fig. 8d): $\delta q_{\mathrm{v}}$ for hydrated parcels is larger in the no-rad calculation than in the all-phys calculation.

In summary, the inf-sed calculation does not capture the presence of hydrated air parcels (by construction). More interestingly, the inf-sed calculation underestimates the magnitude of dehydration for dehydrated air parcels (Fig. 8, left column). In comparison, the no-rad calculation is certainly much closer to the baseline vapour distribution of the cloudy air parcels given by the all-phys calculation. For the dry scenario, the key features of the distribution function of $\delta q_{\mathrm{v}}$ with peaks at large (de)hydration values are well represented by the no-rad calculation (Fig. 8b). However, for the moist scenario, the distribution of $\delta q_{\mathrm{v}}$ deviates significantly between the no-rad and all-phys simulations (Fig. 8d). Furthermore, for both the dry and moist scenarios, there is a large number of air parcels that experience (de)hydration in the all-phys simulations, but almost no change in specific humidity in the no-rad simulations.

## 4 Conclusions

Numerical simulations of cirrus clouds in the tropical tropopause layer (TTL) have been carried out. The redistribution of moisture following the occurrence of the clouds in the simulations is computed from the changes in water vapour over the domain of simulation (Eulerian perspective) and as following air parcels (Lagrangian perspective).

Both microphysical and dynamical processes are important contributors to the net

cloud-induced redistribution of water vapour in the domain. Microphysical processes (ice nucleation and growth, followed by sedimentation and sublimation) always lead to downward transport of water vapour. On the other hand, the direction of the water vapour flux induced by the dynamical processes depends on the moisture content of the cloudy air relative to the environment. The radiative heating induces ascent in the cloudy area and hence upward advection of the cloudy air. When the cloudy air contains more water vapour than the surrounding environment (typically when the environmental air is subsaturated), upward advection of the cloudy air results in an upward flux of water vapour. On the other hand, when the cloud contains less water vapour than the environment (typically when the environmental air is weakly supersaturated), upward advection of the cloudy air results in a downward flux of water vapour.

Regardless of the direction of the net water vapour flux in the Eulerian domain, air parcels that pass through the cloud tops tend to lose water vapour (become dehydrated), and air parcels that pass through the cloud bases tend to gain water vapour (become hydrated). In other words, air parcels that pass through TTL cirrus clouds may undergo either dehydration or hydration. Unless the bases of the cirrus clouds reach below the TTL, the hydrated air parcels remain in the TTL after the life cycle of the clouds. A complete removal of water vapour from the TTL may occur via a sequence of thin cirrus clouds each of which results in a limited downward displacement of hydrated air relative to dehydrated air. Because the hydrated air parcels may remain in the TTL for some time, observations of hydrated parcels despite the absence of convection (such as those reported by Inai et al., 2013) are expected wherever TTL cirrus have redistributed moisture.

Our numerical experiments show that the evolution of the clouds, as well as the degree and spatial extent to which the clouds modify the water vapour profile are very sensitive to the surrounding moisture. This sensitivity to the environmental moisture increases when the dynamical perturbations induced by the cloud radiative heating are considered in the model calculation. Interactions between the clouds and the environment (via which initially cloud-free air becomes cloudy, and vice versa) are enhanced at

the cloud top due to the radiatively induced convective mixing, and at the lateral sides of the clouds due to the vertical shear of the radiatively induced horizontal motions. The numerical results show that both the spatial extent and the magnitude of the cloud-induced redistribution of moisture are underestimated when the radiative-dynamical feedbacks are neglected.

We have also carried out numerical experiments in which most of the complex cloud processes are drastically simplified by assuming instantaneous dehydration to the saturation vapour mixing ratio whenever the homogeneous ice nucleation threshold is reached. That is, upon nucleation, ice crystals take up all moisture in excess of saturation and immediately sediment out of the domain (at an infinite fall speed). This assumption of instantaneous dehydration is sometimes used by simplified and/or large-scale models to compute dehydration of the air in the TTL while avoiding most complications associated with detailed cloud physics. These simplified model runs erroneously fail to capture those regions in which the specific humidity increases. In addition, these simplifications significantly underestimate both the dehydrated area of the clouds and the magnitude of dehydration within the dehydrated area. These results apply to homogeneous ice nucleation, but they may change for heterogeneous nucleation (for which the nucleation threshold is lower).

The simulations have illustrated how the moisture redistribution induced by clouds depends on the (de)hydration process associated with ice sedimentation, the cloud radiative-dynamical feedbacks, and the interactions between the cloudy air and the environment. These processes are expected to affect how clouds modify the water vapour distribution not only for TTL cirrus, but also for other types of clouds in general. These high-resolution simulations demonstrate that the complexity of the cloud-induced moisture redistribution needs to be considered especially for interpretations of high-resolution measurements of water vapour.

*Acknowledgements.* We are grateful to Marat Khairoutdinov for sharing the System of Atmospheric Modelling, and Tak Yamaguchi for sharing the Lagrangian parcel-tracking model. We also would like to thank two anonymous reviewers, whose comments helped improve the

manuscript. This research was supported by the NOAA Climate and Global Change Postdoctoral Fellowship Program (administered by the University Corporation for Atmospheric Research) and by DOE grant SC0006841.

## References

Boehm, M. T. and Verlinde, J.: Stratospheric influence on upper tropospheric tropical cirrus, Geophys. Res. Lett., 27, 3209–3212, doi:10.1029/2000GL011678, 2000.

Böhm, H. P.: A general equation for the terminal fall speed of solid hydrometeors, J. Atmos. Sci., 46, 2419–2427, 1989.

Bougeault, P.: A non-reflective upper boundary condition for limited-height hydrostatic models, Mon. Weather Rev., 111, 420–429, 1983.

Brewer, A. W.: Evidence for a world circulation provided by the measurements of helium and water vapour distribution in the stratosphere, Q. J. Roy. Meteor. Soc., 75, 351–363, 1949.

Chen, Y., Kreidenweis, S. M., McInnes, L. M., Rogers, D. C., and DeMott, P. J.: Single particle analyses of ice nucleating aerosols in the upper troposphere and lower stratosphere, Geophys. Res. Lett., 25, 1391–1394, 1998.

Dinh, T. and Durran, D. R.: A hybrid bin scheme to solve the condensation/evaporation equation using a cubic distribution function, Atmos. Chem. Phys., 12, 1003–1011, doi: 10.5194/acp-12-1003-2012, 2012.

Dinh, T., Durran, D. R., and Ackerman, T.: Maintenance of tropical tropopause layer cirrus, J. Geophys. Res., 115, 1–15, doi:10.1029/2009JD012735, 2010.

Dinh, T., Durran, D. R., and Ackerman, T.: Cirrus and water vapor transport in the tropical tropopause layer -- Part 1: A specific case modeling study, Atmos. Chem. Phys., 12, 9799–9815, doi:10.5194/acp-12-9799-2012, 2012.

Durran, D. R., Dinh, T., Ammerman, M., and Ackerman, T.: The mesoscale dynamics of thin tropical tropopause cirrus, J. Atmos. Sci., 66, 2859–2873, doi:10.1175/2009JAS3046.1, 2009.

Fahey, D. W., Gao, R.-S., Möhler, O., Saathoff, H., Schiller, C., Ebert, V., Krämer, M., Peter, T., Amarouche, N., Avallone, L. M., Bauer, R., Bozóki, Z., Christensen, L. E., Davis, S. M., Durry, G., Dyroff, C., Herman, R. L., Hunsmann, S., Khaykin, S. M., Mackrodt, P., Meyer, J., Smith, J. B., Spelten, N., Troy, R. F., Vömel, H., Wagner, S., and Wienhold, F. G.: The

AquaVIT-1 intercomparison of atmospheric water vapor measurement techniques, Atmos. Meas. Tech. Discuss., 7, 3159–3251, doi:10.5194/amtd-7-3159-2014, 2014.

Forster, P. M. d. F. and Shine, K. P.: Assessing the climate impact of trends in stratospheric water vapor, Geophys. Res. Lett., 29, 1086, doi:10.1029/2001GL013909, 2002.

Fueglistaler, S. and Haynes, P. H.: Control of interannual and longer-term variability of stratospheric water vapor, J. Geophys. Res., 110, 1–14, doi:10.1029/2005JD006019, 2005.

Fueglistaler, S., Bonazzola, M., Haynes, P. H., and Peter, T.: Stratospheric water vapor predicted from the Lagrangian temperature history of air entering the stratosphere in the tropics, J. Geophys. Res., 110, 1–10, 2005.

Fueglistaler, S., Dessler, A. E., Dunkerton, T. J., Folkins, I., Fu, Q., and Mote, P. W.: Tropical tropopause layer, Rev. Geophys., 47, 1–31, doi:10.1029/2008RG000267, 2009.

Fueglistaler, S., Liu, Y. S., Flannaghan, T. J., Haynes, P. H., Dee, D. P., Read, W. J., Remsberg, E. E., Thomason, L. W., Hurst, D. F., Lanzante, J. R., and Bernath, P. F.: The relation between atmospheric humidity and temperature trends for stratospheric water, J. Geophys. Res., 118, 1052–1074, doi:10.1002/jgrd.50157, 2013.

Fujiwara, M., Iwasaki, S., Shimizu, A., Inai, Y., Shiotani, M., Hasebe, F., Matsui, I., Sugimoto, N., Okamoto, H., Nishi, N., Hamada, A., Sakazaki, T., and Yoneyama, K.: Cirrus observations in the tropical tropopause layer over the western Pacific, J. Geophys. Res., 114, doi:10.1029/2008JD011040, 2009.

Gettelman, A., Randel, W. J., Wu, F., and Massie, S. T.: Transport of water vapor in the tropical tropopause layer, Geophys. Res. Lett., 29, 9-1–9-5, doi:10.1029/2001GL013818, 2002.

Hartmann, D. L., Holton, J. R., and Fu, Q.: The heat balance of the tropical tropopause, cirrus, and stratospheric dehydration, Geophys. Res. Lett., 28, 1969–1972, doi:10.1029/2000GL012833, 2001.

Hoskins, B. J.: Towards a PV-$\theta$ view of the general circulation, Tellus A, 43, 27–35, 1991.

Immler, F., Krüger, K., Fujiwara, M., Verver, G., Rex, M., and Schrems, O.: Correlation between equatorial Kelvin waves and the occurrence of extremely thin ice clouds at the tropical tropopause, Atmos. Chem. Phys., 8, 4019–4026, 2008.

Inai, Y., Hasebe, F., Fujiwara, M., Shiotani, M., Nishi, N., Ogino, S.-Y., Vömel, H., Iwasaki, S., and Shibata, T.: Dehydration in the tropical tropopause layer estimated from the water vapor match, Atmos. Chem. Phys., 13, 8623–8642, doi:10.5194/acp-13-8623-2013, 2013.

James, R., Bonazzola, M., Legras, B., Surbled, K., and Fueglistaler, S.: Water vapor transport and dehydration above convective outflow during Asian monsoon, Geophys. Res. Lett., 35,

L20 810, doi:10.1029/2008GL035441, 2008.
Jensen, E. and Pfister, L.: Transport and freeze-drying in the tropical tropopause layer, J. Geophys. Res., 109, 1–16, 2004.
Jensen, E. J., Smith, J. B., Pfister, L., Pittman, J. V., Weinstock, E. M., Sayres, D. S., Herman, R. L., Troy, R. F., Rosenlof, K., Thompson, T. L., Fridlind, A. M., Hudson, P. K., Cziczo, D. J., Heymsfield, A. J., Schmitt, C., and Wilson, J. C.: Ice supersaturations exceeding 100% at the cold tropical tropopause : implications for cirrus formation and dehydration, Atmos. Chem. Phys., 5, 851–862, 2005.
Khairoutdinov, M. F. and Randall, D. A.: Cloud resolving modeling of the ARM summer 1997 IOP: Model formulation, results, uncertainties, and sensitivities., J. Atmos. Sci., 60, 607–625, 2003.
Klemp, J. B. and Durran, D. R.: An upper boundary condition permitting internal gravity wave radiation in numerical mesoscale models, Mon. Weather Rev., 111, 430–444, 1983.
Koop, T., Luo, B., Tsias, A., and Peter, T.: Water activity as the determinant for homogeneous ice nucleation in aqueous solutions, Nature, 406, 611–614, 2000.
Liu, Y. S., Fueglistaler, S., and Haynes, P. H.: Advection-condensation paradigm for stratospheric water vapor, J. Geophys. Res, 115, 1–18, 2010.
Mace, G. G., Zhang, Q., Vaughan, M., Marchand, R., Stephens, G., Trepte, C., and Winker, D.: A description of hydrometeor layer occurrence statistics derived from the first year of merged Cloudsat and CALIPSO data, J. Geophys. Res., 114, 1–17, doi:10.1029/2007JD009755, 2009.
Massie, S., Gettelman, A., Randel, W., and Baumgardner, D.: Distribution of tropical cirrus in relation to convection, J. Geophys. Res., 107, doi:10.1029/2001JD001293, 2002.
Randel, W. J. and Jensen, E. J.: Physical processes in the tropical tropopause layer and their roles in a changing climate, Nat. Geosci., 6, 169–176, doi:10.1038/ngeo1733, 2013.
Ren, C., MacKenzie, A. R., Schiller, C., Shur, G., and Yushkov, V.: Diagnosis of processes controlling water vapour in the tropical tropopause layer by a Lagrangian cirrus model, Atmos. Chem. Phys., 7, 5401–5413, doi:10.5194/acp-7-5401-2007, 2007.
Solomon, S., Garcia, R. R., Rowland, S. F., and Wuebbles, D. J.: On the depletion of Antarctic ozone, Nature, 321, 755–758, 1986.
Solomon, S., Rosenlof, K. H., Portmann, R. W., Daniel, J. S., Davis, S. M., Sanford, T. J., and Plattner, G.-K.: Contributions of stratospheric water vapor to decadal changes in the rate of global warming, Science, 327, 1219–1223, 2010.
Spichtinger, P. and Krämer, M.: Tropical tropopause ice clouds: a dynamic approach to

**Table 1.** The number of air parcels that pass by the cloud during the period of integration $N_c$, and the fraction of parcels within the set $N_c$ that are dehydrated and hydrated in all model simulations.

| Scenario | Case | $\frac{N^-}{N_c}$ | $\frac{N^+}{N_c}$ |
|---|---|---|---|
| Dry | all-phys | $0.43$ | $0.53$ |
| $N_c = 2.4 \times 10^4$ | no-rad | $0.31$ | $0.42$ |
| | inf-sed | $0.26$ | $0$ |
| Moist | all-phys | $0.47$ | $0.37$ |
| $N_c = 8.2 \times 10^4$ | no-rad | $0.24$ | $0.27$ |
| | inf-sed | $0.14$ | $0$ |

the mystery of low crystal numbers, Atmos. Chem. Phys., 13, 9801–9818, doi:10.5194/acp-13-9801-2013, 2013.

Virts, K. S. and Wallace, J. M.: Annual, interannual, and intraseasonal variability of tropical tropopause transition layer cirrus, J. Atmos. Sci., 67, 3097–3112, 2010.

Wang, P.-H., Minnis, P., McCormick, M. P., Kent, G. S., and Skeens, K. M.: A 6-year climatology of cloud occurrence frequency from Stratospheric Aerosol and Gas Experiment II observations (1985–1990), J. Geophys. Res., 101, 29 407–29 429, doi:10.1029/96JD01780, 1996.

Wang, T. and Dessler, A. E.: Analysis of cirrus in the tropical tropopause layer from CALIPSO and MLS data: A water perspective, J. Geophys. Res., 117, 1–10, doi:10.1029/2011JD016442, 2012.

Yamaguchi, T. and Randall, D. A.: Cooling of Entrained Parcels in a Large-Eddy Simulation, J. Atmos. Sci., 69, 1118–1136, doi:10.1175/JAS-D-11-080.1, 2012.

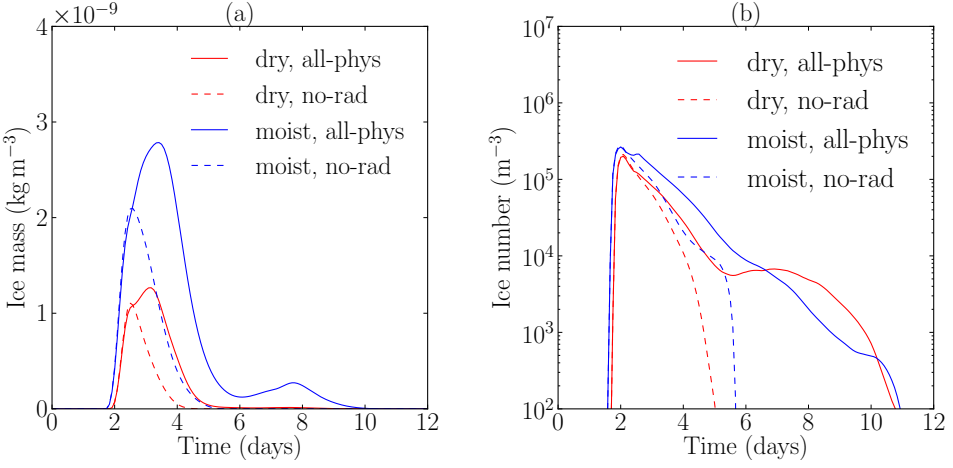


**Fig. 1.** Evolution of **(a)** the domain-averaged ice mass and **(b)** the ice number density averaged over the cloudy area (not over the entire domain) in the no-rad and all-phys simulations for both the dry and moist scenarios.

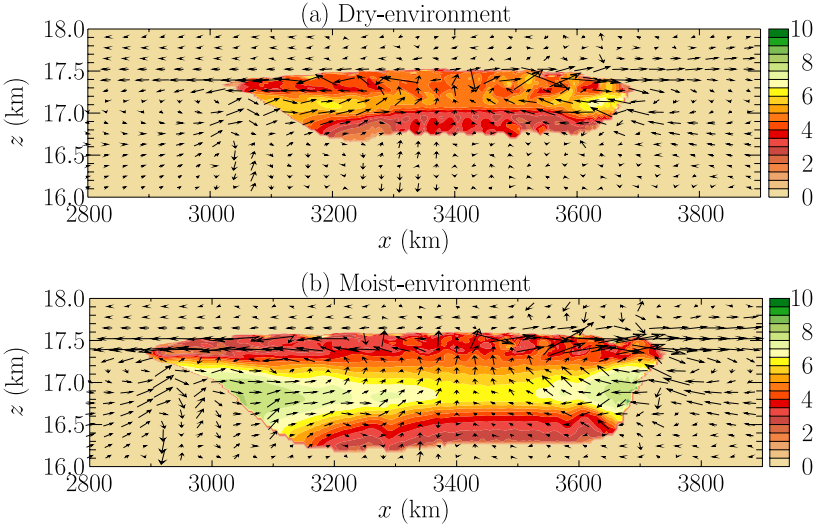


**Fig. 2.** Mean crystal radius (μm) at $t = 3.5$ d in the all-phys simulations in the dry (top panel) and moist (bottom panel) scenarios. Vectors show the radiatively induced motions.

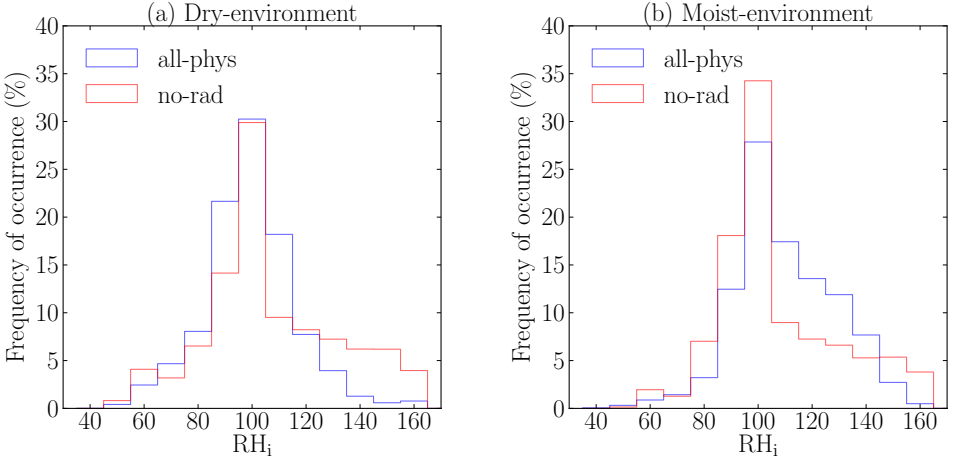


**Fig. 3.** Frequency distribution of in-cloud relative humidities over the cloud lifetimes.

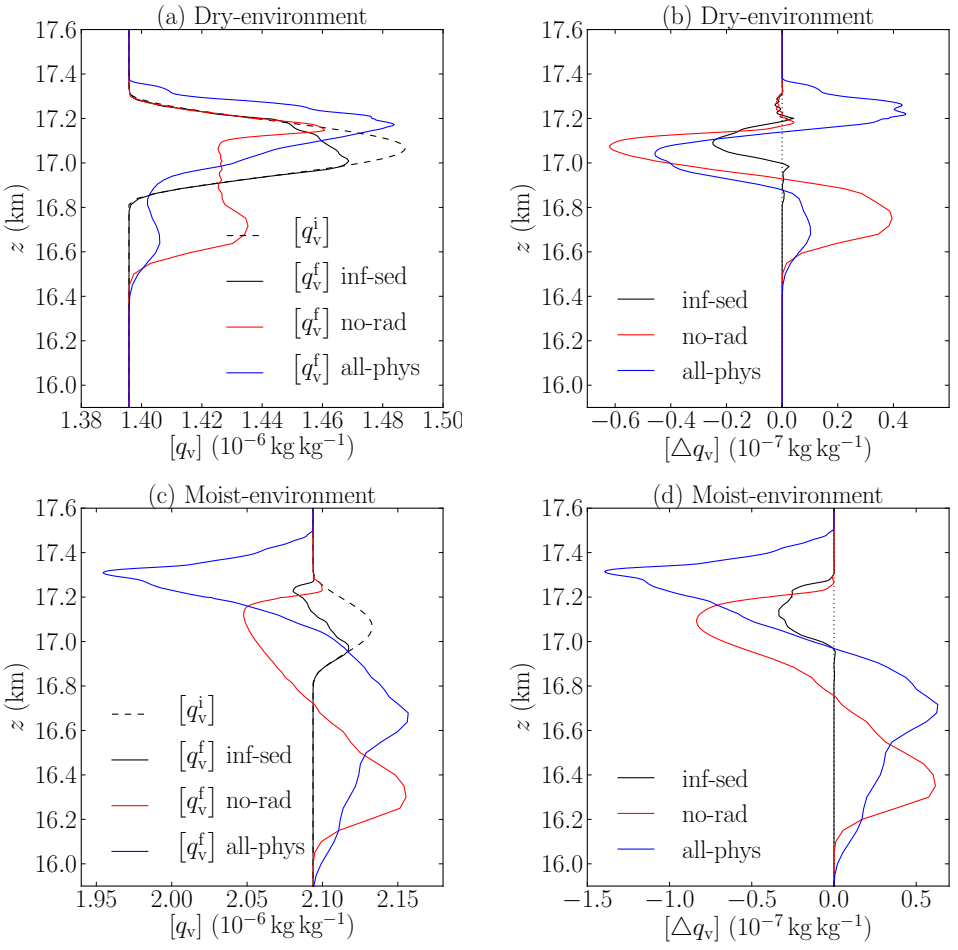


**Fig. 4.** The horizontal-domain average of the initial and final water vapour mixing ratio $q_v$ (left column), and changes in $q_v$ (right column) in the dry (top panels) and moist (bottom panels) scenarios.

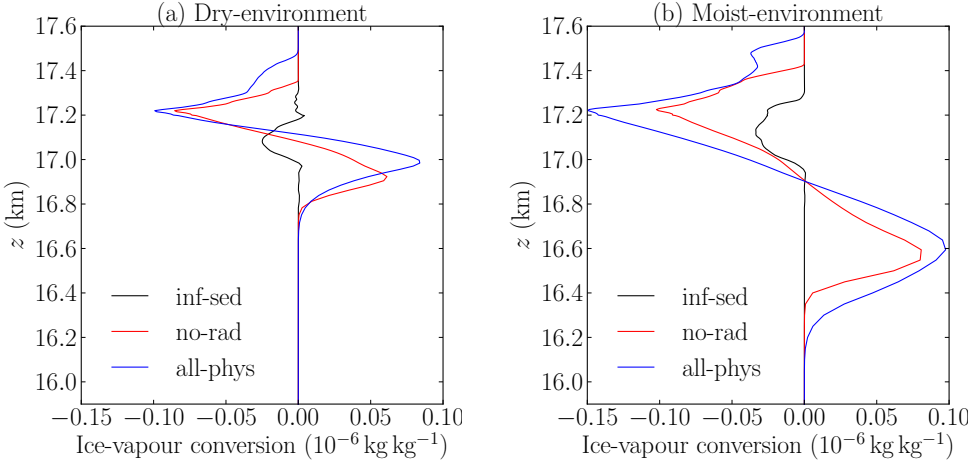


**Fig. 5.** The profiles of accumulative mass exchange from ice to vapour over the model integration.

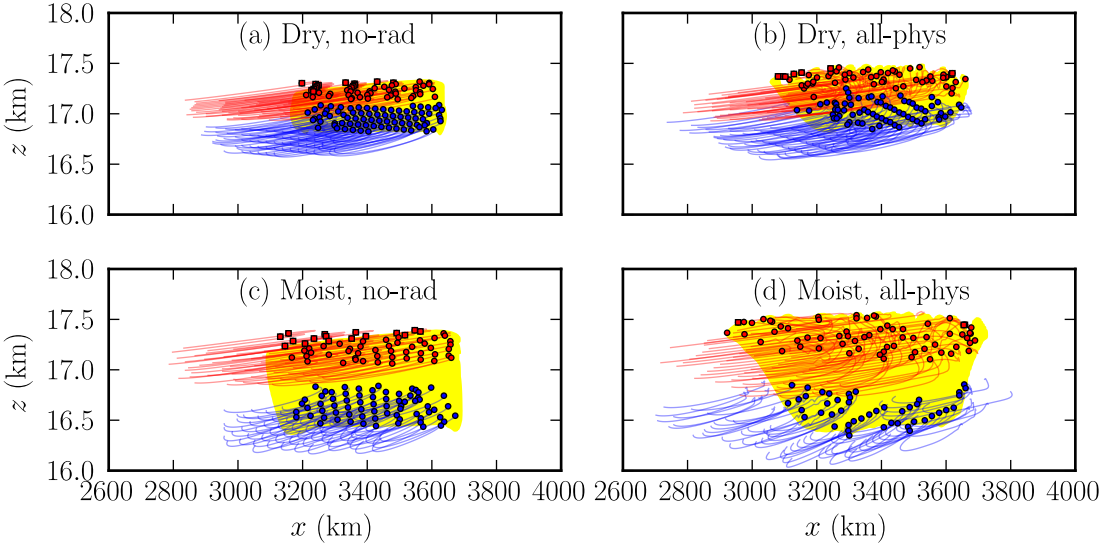


**Fig. 6.** The cloud at $t = 3.5$ d (yellow-shaded region), and representative air parcels' trajectories from $t = 0$ to $3.5$ d in the no-rad and all-phys simulations for the dry (top row) and moist (bottom row) scenarios. Trajectories for dehydrated and hydrated air parcels are shown respectively in red and blue. The locations of the parcels at $3.5$ d are marked with circles if the parcels are inside the cloudy region, and with squares if the parcels passed through the cloud at earlier times and are in cloud-free air at $3.5$ d. Some parcels (whose locations at $3.5$ d are not indicated by squares or circles) have not entered the cloud (but will do so after $3.5$ d).

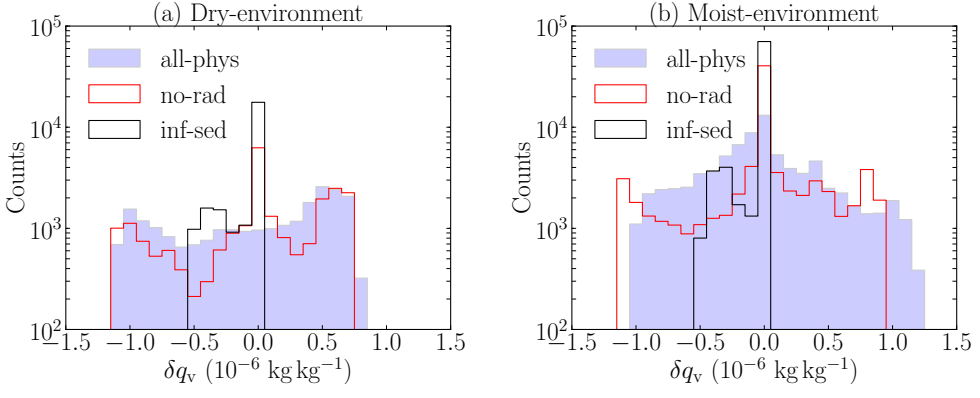


**Fig. 7.** Histograms (in log scale) of changes in specific humidity over the integration (final minus initial) of all cloudy air parcels (for which $q_i > 5 \times 10^{-8}$ kg kg$^{-1}$ in at least one of the runs: all-phys and no-rad).

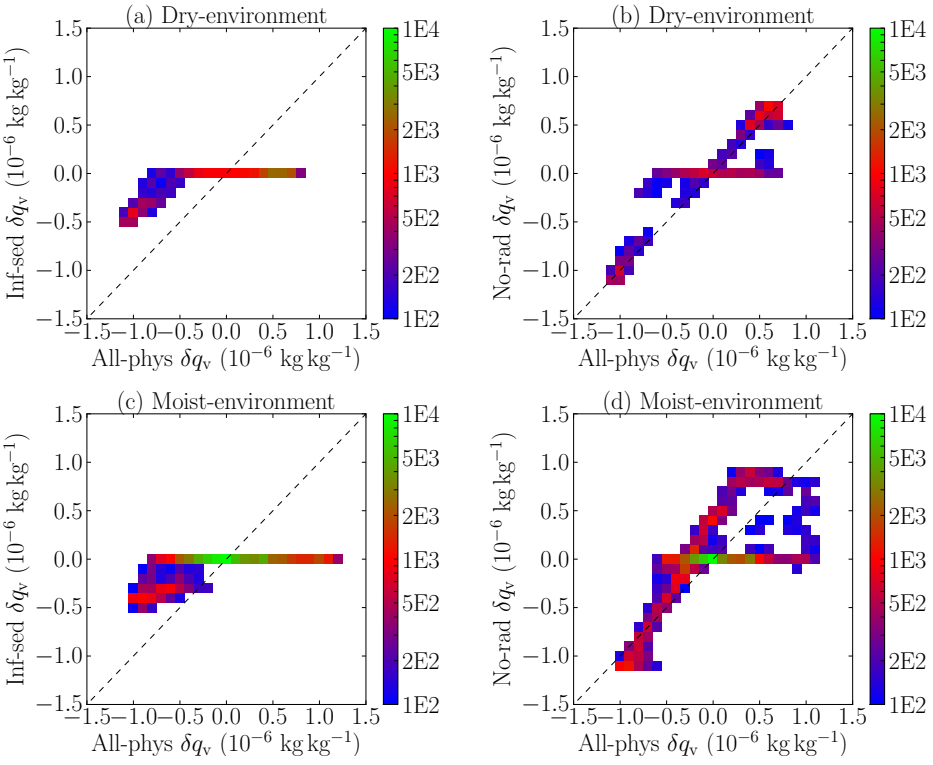


**Fig. 8.** The changes in specific humidity of the cloudy air parcels comparing between the inf-sed and all-phys simulations (left column), and between the no-rad and all-phys simulations (right column) for the dry (top row) and moist (bottom row) scenarios. The baseline water vapour distribution is taken from the all-phys simulations and is plotted in the horizontal axis in all four panels. The dashed line shows the one-to-one slope. The colour bar shows the number of air parcel counts.